GDCh

Research Article

Angewandte
Chemie
International Edition
www.angewandte.org

VIP **Peptide Biomaterials** *Very Important Paper*

Chaperone-Derived Copper(I)-Binding Peptide Nanofibers Disrupt Copper Homeostasis in Cancer Cells

M. T. Jeena, Julian Link, Jian Zhang, Iain Harley, Petri Turunen, Robert Graf,
Manfred Wagner, Luis Andre Baptista, Hendrik R. A. Jonker, Liyang Cui, Ingo Lieberwirth,
Katharina Landfester, Jianghong Rao,* David Y. W. Ng,* and Tanja Weil*

Abstract: Copper (Cu) is a transition metal that plays crucial roles in cellular metabolism. Cu^+ homeostasis is upregulated in many cancers and contributes to tumorigenesis. However, therapeutic strategies to target Cu^+ homeostasis in cancer cells are rarely explored because small molecule Cu^+ chelators have poor binding affinity in comparison to the intracellular Cu^+ chaperones, enzymes, or ligands. To address this challenge, we introduce a Cu^+ chaperone-inspired supramolecular approach to disrupt Cu^+ homeostasis in cancer cells that induces programmed cell death. The Nap-FFMTCGGCR peptide self-assembles into nanofibers inside cancer cells with high binding affinity and selectivity for Cu^+ due to the presence of the unique MTCGGC motif, which is conserved in intracellular Cu^+ chaperones. Nap-FFMTCGGCR exhibits cytotoxicity towards triple negative breast cancer cells (MDA-MB-231), impairs the activity of Cu^+ dependent co-chaperone super oxide dismutase1 (SOD1), and induces oxidative stress. In contrast, Nap-FFMTCGGCR has minimal impact on normal HEK 293T cells. Control peptides show that the self-assembly and Cu^+ binding must work in synergy to successfully disrupt Cu^+ homeostasis. We show that assembly-enhanced affinity for metal ions opens new therapeutic strategies to address disease-relevant metal ion homeostasis.

[*] Dr. M. T. Jeena, J. Link, J. Zhang, I. Harley, Dr. R. Graf,
Dr. M. Wagner, Dr. L. A. Baptista, Dr. I. Lieberwirth,
Dr. K. Landfester, Dr. D. Y. W. Ng, Prof. Dr. T. Weil
Max-Planck-Institut für Polymerforschung
Ackermannweg 10, 55128 Mainz, Germany
E-mail: tweil@mpip-mainz.mpg.de
        david.ng@mpip-mainz.mpg.de

Dr. L. Cui, Dr. J. Rao
Department of Radiology
Molecular Imaging Program at Stanford
School of Medicine
Stanford University
Stanford, CA 94305, USA
E-mail: jrao@stanford.edu

Dr. P. Turunen
Zentrale Einrichtung für Mikroskopie
Institut für Molekulare Biologie (IMB)
Johannes Gutenberg-Universität
Ackermannweg 4, 55128 Mainz, Germany

Dr. H. R. A. Jonker
Institut für Organische Chemie und Chemische Biologie
Biomolekulares Magnetresonanz Zentrum (BMRZ)
Goethe Universität Frankfurt
60438 Frankfurt am Main, Germany

Introduction

Metal ions are indispensable for multiple cellular functions including signal transduction, chemical reactions, and structural components of biomacromolecules.[1] Copper (Cu) is a redox-active transition metal serving as an enzyme co-factor mediating metabolic processes essential for cellular growth and development including antioxidant defense,[2] aerobic respiration,[3] iron transport,[4] and other processes such as pigment synthesis.[5] The availability of intracellular, unbound Cu ions is controlled tightly to avoid oxidative stress, lipid peroxidation and non-specific binding to intracellular biomolecules.[6,7] Therefore, the concentration of free Cu ions in the cytoplasm is kept exceptionally low.[8] To maintain cellular Cu homeostasis, cells have evolved sophisticated trafficking pathways consisting of transporters, ligands, chaperones, and their respective counter proteins (co-chaperones).[9,10]

Extracellular Cu^{2+} is reduced to Cu^+ by the six transmembrane epithelial antigen of prostate (STEAP) family metalloreductase proteins located in the plasma membrane.[11] Then, cellular uptake is mediated by the high affinity Cu^+ transmembrane transporter protein Ctr1 (SLC31 A1).[12] The predominant oxidation state of Cu in the cell is +1 due to the reductive cellular environment.[13] Once Cu^+ is transported into the cell, cytosolic GSH binds free Cu^+ and forms Cu^+-GSH complex to minimize the availability of free Cu^+ ions and to create an exchangeable pool of Cu^+.[8] The Cu^+-GSH complex transfers Cu^+ to the cytosolic Cu^+ chaperones, such as antioxidant 1 (Atox1), cyclooxygenase17 (COX17) and copper chaperone for

superoxide dismutase (CCS).[14,15] The Cu$^+$ trafficking pathways in human cells consist of high chaperone-protein specificity following an affinity gradient.[16] Briefly, Cu$^+$ transfer takes place from Atox1 to ATPase Cu$^+$ transporting alpha/beta (ATP7 A/7B) located at the trans-Golgi network, from COX17 to mitochondrial synthesis of cytochrome oxidase 1/2 (Sco1/2) or cytochrome C oxidase (CCO), and from CCS to super oxide dismutase1 (SOD1) located in the cytosol or in the mitochondrial inner membrane (Figure 1A).[17] Some chaperones (*eg.*, Atox1 and CCS) and co-chaperones (*eg.*, ATP 7 A/7B) bind to Cu$^+$ via the cysteine residues of a conserved **MXCXXC** (**X** is an arbitrary amino acid) domain and Cu$^+$ exchange proceeds through a thiol exchange mechanism (Figure 1A).[18] Methio-

nine was also shown from model peptide studies to be important in conferring additional binding stability[19].

Imbalances in Cu$^+$ homeostasis induces abnormalities, which are indicated in the pathogenesis of several diseases including cancer,[20] Wilson disease (WD),[21] and Menkes disease.[22] For example, Cu$^+$ is involved in cancer cell proliferation, immune system modulation and angiogenesis of the tumor growth and development,[23] including colorectal,[24] lung,[25] breast,[26] primary brain,[27] hepatocellular carcinoma[28] etc. Recently, a new concept of "cuproplasia" has been introduced, defined as Cu-dependent cell growth and proliferation, which can be pharmacologically targeted by Cu-selective chelators or activated by ionophores as a target for cancer therapy.[29] However, the design of new molecules capable of chelating intracellular Cu$^+$ is
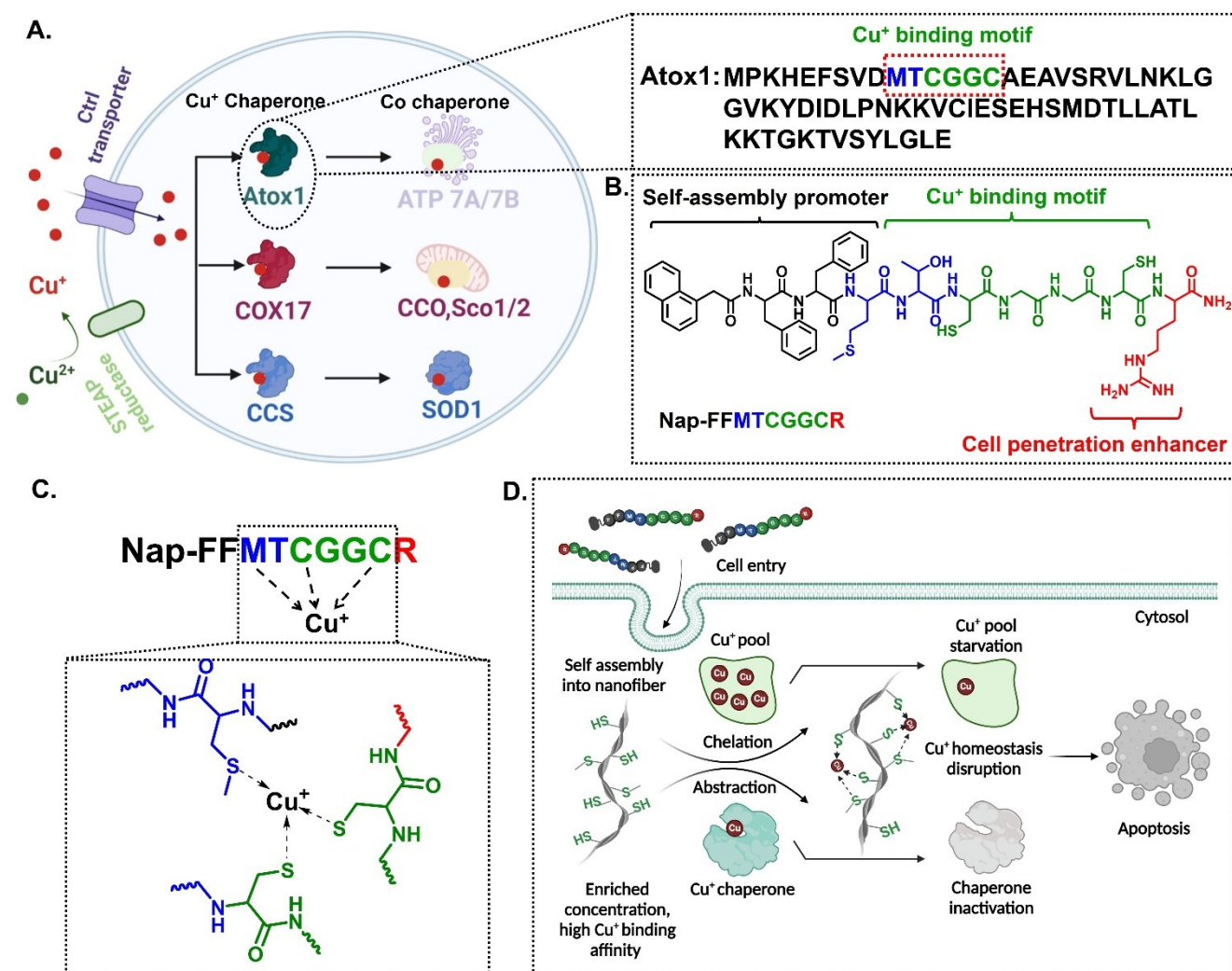

Figure 1. Schematic illustration of **(A)** Cu$^+$ uptake and trafficking in human cells. Complete sequence of human Atox1 possessing MTCGGC as Cu$^+$-binding domain is shown. **(B)** Chemical structure of Cu$^+$ chaperone-derived Nap-FFMTCGGCR peptide consisting of MTCGGC as a Cu$^+$ binding motif, arginine (R) as a cellular uptake enhancer and Nap-FF as a self-assembly promoter. **(C)** Schematic illustration showing the proposed coordination model of Nap-FFMTCGGCR binding to Cu$^+$.Nap-FFMTCGGCR binds Cu$^+$ primarily through the thiol groups of the cysteine residue in a 1:1 stoichiometric ratio. Methionine (M) contributes to this coordination **(D)** Nap-FFMTCGGCR self-assembles into nanofibers upon the entry inside the MDA-MB-231 breast cancer cells providing multiple Cu$^+$-binding motifs at the nanofiber surface. Cu$^+$ binding disrupts Cu$^+$ trafficking in cancer cells. Nap-FFMTCGGCR fibers capture Cu$^+$ ions from the intracellular pool or Cu$^+$ chaperones, presumably resulting in an overall deprivation of Cu$^+$ bioavailability, which induces oxidative stress, cellular dysfunction, and ultimately apoptosis.

extremely challenging as Cu^+ binding affinity in the femtomolar range is required to effectively interfere with chaperone/co-chaperone Cu^+ binding.[15]

Using the conserved **MTCGGC** motif of human Atox1 Cu^+ chaperone, we propose that multiple copies of the motif arranged within a superstructure network should exhibit assembly-enhanced affinity for Cu^+ (Figure 1A–B). Human Atox1 binds Cu^+ using the cysteine residues of **MTCGGC** motif, adopting a two coordinate S–Cu–S model with a S–Cu distance of 2.16 Å.[30] Hence, we designed the self-assembling peptide amphiphile **Nap-FFMTCGGCR** comprising three motifs, (1) the naphthalene (**Nap**) capped diphenylalanine (**FF**) domain that promotes self-assembly, (2) the sequence **MTCGGC** binding Cu^+ with high affinity and selectivity for Cu^+ versus other cations, and (3) the arginine (**R**) residue to enhance cellular uptake. **Nap-FFMTCGGCR** is proposed to bind Cu^+ primarily through the cysteine residues, assisted by methionine within the **MTCGGC** motif (Figure 1C).[19,31] Upon internalization, the local enrichment[32] promotes the assembly into cytosolic **Nap-FFMTCGGCR** fibers where they can bind and competitively acquire Cu^+ from the intracellular proteins, ligands, or pools, which induces cellular dysfunctions leading to apoptosis (Figure 1D). Control peptides that cannot self-assemble underline the importance of fibril formation to achieve the desired function. Selectivity towards Cu-sensitive cancer cells such as triple negative breast cancer cells, MDA-MB-231, has been investigated and compared against normal HEK 293T cells.

We show that *in situ* assembly strategies can be used as a powerful tool to enhance biochemical properties. To date, diverse intracellular components overexpressed in cancer cells, such as receptors, enzymes etc. have been explored to induce *in situ* self-assembly of amphiphilic peptides within cancer cells, leading to cellular dysfunction and ultimately causing cell death.[33,34] For example, Liu *et al.* utilized the over expression of GSH to generate self-sorted peptide assemblies inside HeLa cells, targeting the endoplasmic reticulum and Golgi apparatus simultaneously.[35,36] Guo *et al.* showed that peptide-protein association in living cells triggered necroptosis in colorectal cancer.[37] Here, we present, for the first time, the disruption of intracellular metal ion homeostasis using artificial *in situ* generated self-assembly to trigger apoptosis of triple negative breast cancer cell.

Results and Discussion

Design, Synthesis, and Cu^+ Binding of Nap-FFMTCGGCR

Derived from the natural Cu^+ chaperones, the sequence **MTCGGC** is designed featuring two cysteine residues spaced by two glycine residues, responsible for Cu^+ binding. The N-terminus of **MTCGGC** is modified with a naphthalene-capped diphenylalanine (**Nap-FF**), that provides hydrophobicity and π–π interactions to promote self-assembly into nanofibers. The C-terminus is extended with an arginine (**R**) to facilitate cell membrane interactions and

cellular uptake. The **FFMTCGGCR** sequence was synthesized using fluorenylmethoxycarbonyl (Fmoc) solid phase peptide synthesis (SPPS) on rink amide resin. The N-terminus of the peptide was coupled to naphthalene acetic acid using 2-(1H-benzotriazole-1-yl)-1,1,3,3-tetramethyluronium hexafluorophosphate (HBTU)/N, N-di*iso*propylethylamine (DIPEA) on resin (Figure S1). The **Nap-FFMTCGGCR** was removed from the solid support using a cleavage cocktail based on trifluoroacetic acid (TFA). The cleaved peptide was purified using high-performance liquid chromatography (HPLC) and characterized by electron spray ionization-mass spectrometry (ESI-MS) (Figure S2), ^{1}H NMR (Figure S3) and ^{1}H, ^{1}H-COSY NMR spectroscopy (Figure S4).

Nap-FFMTCGGCR^{mn} (The superscript "*mn*" represents the monomeric form of the peptide) can be dissolved in solvents including DMSO, methanol, and water/acetonitrile mixture. Its critical aggregation concentration (CAC) in Milli-Q water is 50 μM as measured using Nile red (Figure S5). As the predominant oxidation state of Cu inside the cell is +1 due to the reductive intracellular environment,[38] we used Cu^+ throughout our investigation from the source $Cu[(CH_3CN)_4]PF_6$.[39] First, we studied the Cu^+ binding of **Nap-FFMTCGGCR^{mn}** at the molecular level. The **Nap-FFMTCGGCR^{mn}** absorbs at 254–300 nm, which showed an increase in the intensity upon the mol. equivalent addition of Cu^+ (Figure 2A). The Cu^+ bound fraction of **Nap-FFMTCGGCR^{mn}** calculated from the UV/Vis spectra suggests ~1:1 stoichiometric binding of **Nap-FFMTCGGCR^{mn}** to Cu^+ (Table S1). The molecular mass analysis by MALDI-TOF further supported the formation of **Cu^+-Nap-FFMTCGGCR^{mn}** with the appearance of respective molecular mass at 1248.4 (m/z), matching the calculated mass of the Cu^+ bound peptide (Figure S6). The Ellman's reagent (5, 5'-dithiobis (2-nitrobenzoic acid), DTNB) assay was conducted to investigate the involvement of sulfhydryl (−SH) functional groups of **Nap-FFMTCGGCR^{mn}** binding to Cu^+.[40] DTNB reacts with free -SH to produce a mixed disulfide and 2-nitro-5-thiobenzoic acid (TNB). TNB absorbs at 412 nm allowing free -SH groups to be determined quantitatively.

Stoichiometric addition of Cu^+ to **Nap-FFMTCGGCR^{mn}** caused a decrease in the free -SH concentration of **Nap-FFMTCGGCR^{mn}** in which $23.8\pm5.3\,\%$, $52.1\pm1.4\,\%$, $87.3\pm0.89\,\%$ and $89.2\pm0.98\,\%$ decrease was observed at 0.25, 0.5, 1 and 2 mol. equivalent addition of Cu^+ respectively (Figure 2B–C, Figure S7). These results reveal the involvement of -SH functional group on binding to Cu^+.

Next, we analyzed Cu^+ binding of **Nap-FFMTCGGCR^{mn}** by ^{1}H NMR. First, the structure of **Nap-FFMTCGGCR^{mn}** was characterized by ^{1}H NMR in DMSO-d$_6$ as the solvent, as depicted in Figure S3. Next, Cu^+ binding to **Nap-FFMTCGGCR^{mn}** was studied by ^{1}H NMR in MeOH-d$_4$, which was necessary to prevent oxidation of the peptide. We observed a progressive loss of ^{1}H NMR signal intensity upon the stoichiometric addition of Cu^+ to **Nap-FFMTCGGCR^{mn}** accompanied by broadening of the peaks as depicted in Figure S8. This observation supports binding of Cu^+ to **Nap-FFMTCGGCR^{mn}**.[41] Quantitative analysis of the NMR
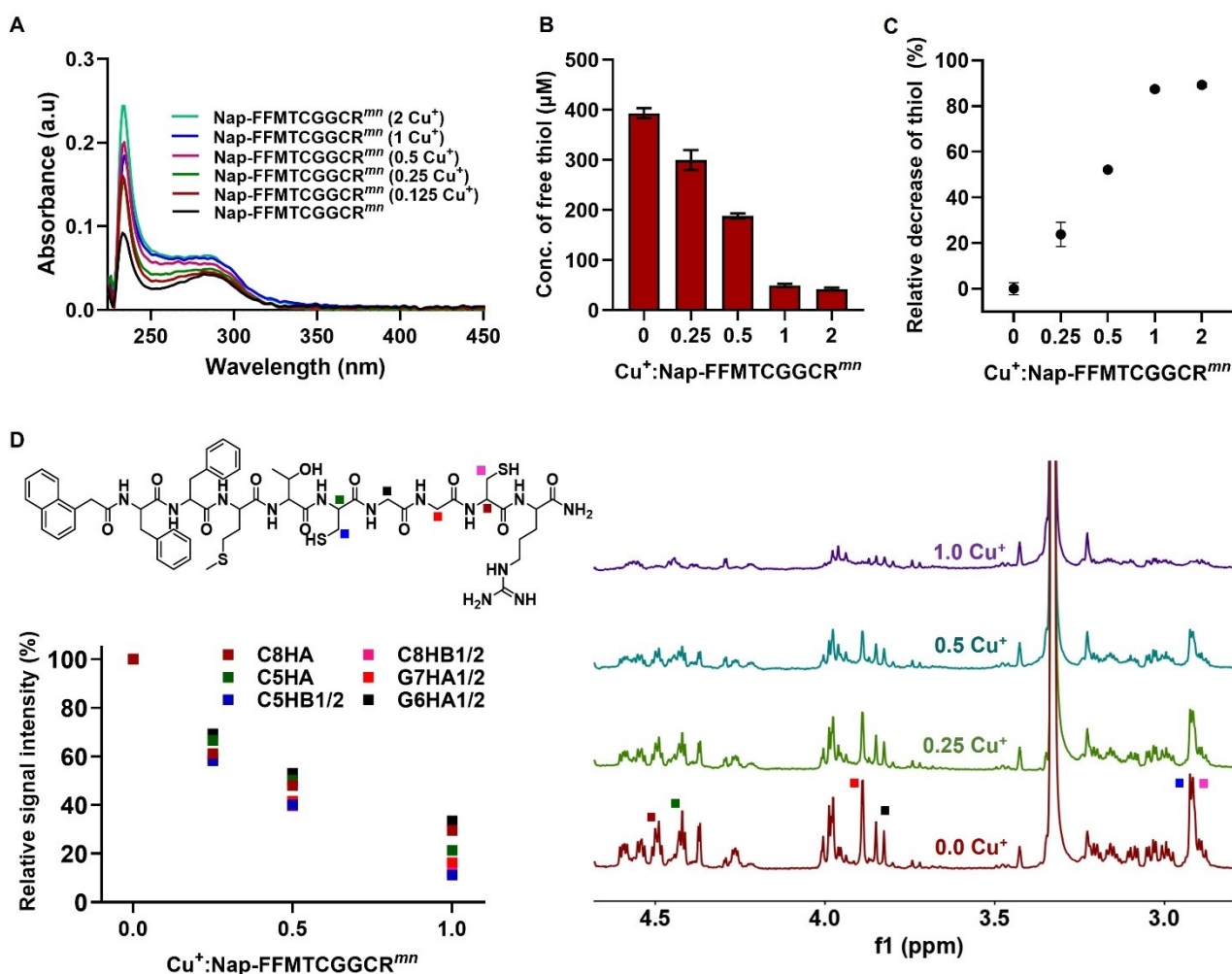
Figure 2. (A) The UV/Vis spectra of Nap-FFMTCGGCR^{mn} (10 μM, Milli-Q water) in response to the addition of Cu$^+$ (0, 0.25, 0.5, 1 and 2 mol. equivalent). **(B)** Ellman's reagent assay showing the decrease of free -SH concentration upon the addition of Cu$^+$ (0, 0.25, 0.5, 1 and 2 mol. equivalent) to Nap-FFMTCGGCR^{mn} (MeOH, 400 μM). **(C)** Relative decrease of free -SH concentration calculated from Figure B. **(D)** Relative signal intensity obtained after the addition of Cu$^+$ (0, 0.25, 0.5 and 1 mol. equivalent) to Nap-FFMTCGGCR^{mn} calculated from the ^{1}H NMR spectra (700 MHz, 298 K, MeOH-d$_4$) with respect to an internal standard (C$_2$H$_2$Cl$_4$). Corresponding ^{1}H NMR spectra (zoom in) and protons of interests are shown. The data represented as mean ± s.d., $n = 3$ for B, C and D.

signal intensity with respect to the internal standard C$_2$H$_2$Cl$_4$ (at 6.49 ppm) was performed and the results were summarized in Figure S9 and Figure 2D. Upon the addition of 0.5 mol. equivalent Cu$^+$, the signal intensity of protons C5HA (4.43 ppm), C5HB1/2 (2.9 ppm), C8HA (4.49 ppm), C8HB1/2 (2.89 ppm), G6HA1/2 (3.84 ppm) and G7HA1/2 (3.9 ppm) decreased, from 100 % without Cu$^+$, to 46.0 ± 0.23 %, 37.3 ± 0.08 %, 44.3 ± 0.3 %, 36.8 ± 0.1 %, 48.4 ± 0.3 % and 38.3 ± 0.2 %, respectively. Upon addition of one mol. equivalent Cu$^+$, the signal intensity of the respective protons further decreased to 23.5 ± 0.5 %, 9.9 ± 0.2 %, 14.5 ± 0.3 %, 10.7 ± 0.2 %, 30.1 ± 0.3 %, 11.3 ± 0.3 %. These results support that the **CGGC** motif was likely involved in binding to Cu$^+$. In particular, the signal intensities of the β-protons of the cysteine residues were reduced significantly after the addition of equimolar Cu$^+$ (Figure 2D), whereas the signal

intensities of the aromatic protons (*i.e.* F2HD1/2 at 7.0 ppm, 39.4 ± 0.2 %) were less affected (Figure S10).

Furthermore, their integrals did not show any obvious changes with respect to the reference, suggesting that no aggregation occurred within the tested period of up to 24 h (Figure S11). From these observations, we postulate that Cu$^+$ binding to **Nap-FFMTCGGCR**^{mn} should result in a restricted mobility of **Nap-FFMTCGGCR**^{mn} leading to the loss of proton signals. Further, the EPR spectra showed no signal corresponding to Cu^{2+} indicating the stability of Cu$^+$ upon binding to **Nap-FFMTCGGCR**^{mn} within 24 h (Figure S12). The **Nap-FFMTCGGCR**^{mn} peptide showed high specificity towards Cu$^+$ and no obvious response to other physiologically relevant metal ions such as K$^+$, Ca^{2+}, Zn^{2+}, Co^{2+}, Fe^{2+}, and Mg^{2+} was observed, except towards Cu^{2+} (Figure S14).

Nap-FFMTCGGCR^{ag} Efficiently Bind Cu^+

Next, we studied Cu^+ binding to **Nap-FFMTCGGCR**^{ag} (the superscript "*ag*" refers to peptides in their aggregated state) above the CAC of 50 µM in Milli-Q water. The CAC remained unchanged after the addition of Cu^+ (1 mol. equivalent) as shown in Figure S15. The transmission electron microscopy (TEM) and liquid-tapping atomic force microscopy (AFM) showed that **Nap-FFMTCGGCR**^{ag} self-assembled into ordered nanofibers (Figure S15). The diameter of the nanofibers measured from TEM images was 9.1 ± 0.3 nm, and AFM images revealed a height of 6.2 ± 0.5 nm. Cryo electron microscopy (Cryo-EM) further confirmed the

fiber formation of **Nap-FFMTCGGCR**^{ag}, with an average diameter of 9 ± 0.3 nm and several micrometers in length (Figure 3A, Figure S16) that slightly increased to 9.9 ± 0.3 nm after binding to Cu^+ (Figure 3C, Figure S17). The UV/Vis spectra revealed an increase in the absorption at 254-300 nm after binding to Cu^+ (Figure S20). The secondary structure conformation of the **Nap-FFMTCGGCR**^{ag} was assessed using circular dichroism (CD) spectroscopy. The spectra showed a strong negative cotton effect at 233 nm, a positive cotton effect at 212 nm, and a negative cotton effect at 203 nm indicating the presence of cation-π interactions, β-sheets, and α-helix conformation respectively, which are retained after binding to equimolar Cu^+ (Fig-
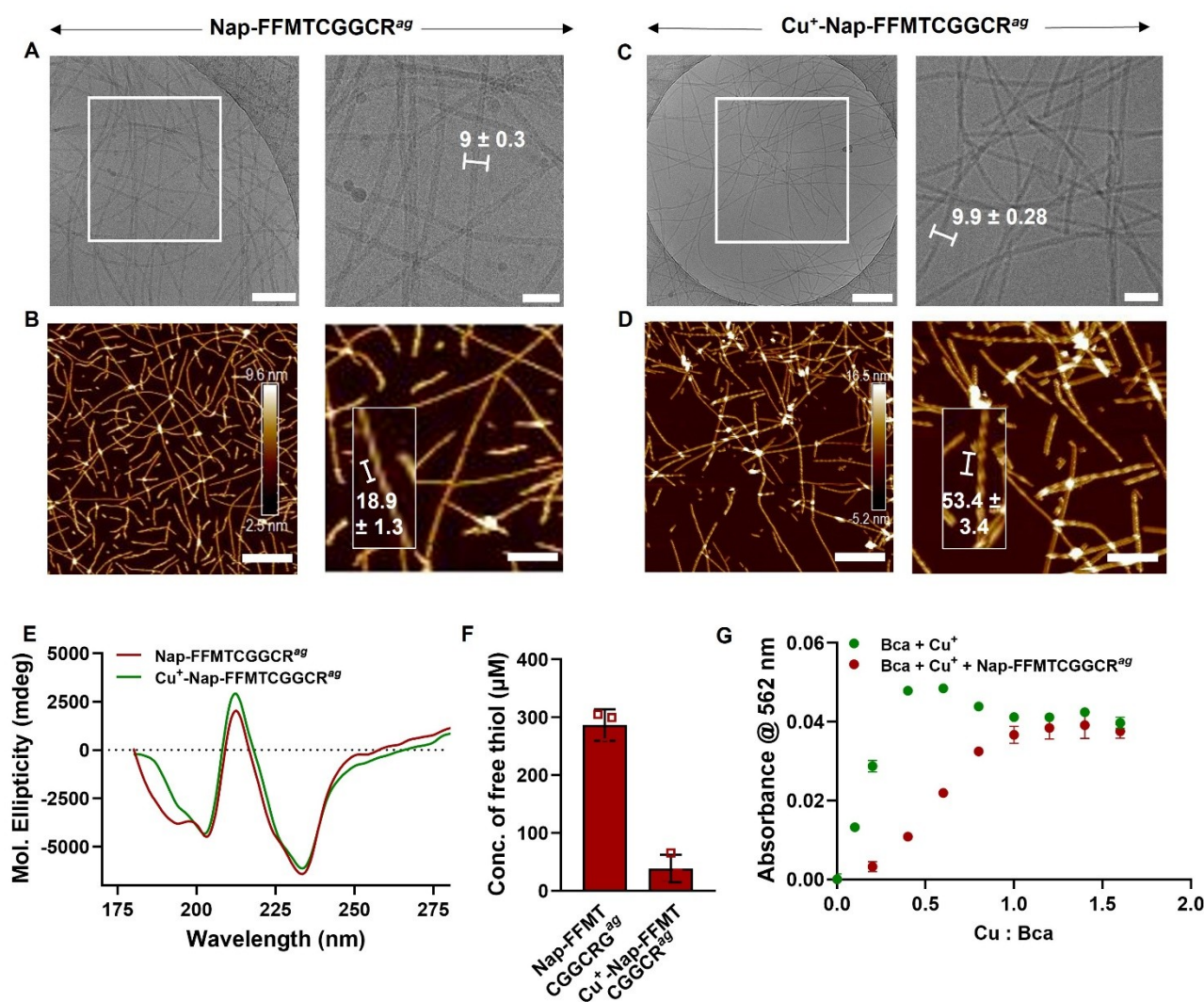

Figure 3. The microscopy images of **(A)** Nap-FFMTCGGCR^{ag} (100 µM, Milli-Q) observed under Cryo-EM (scale bar: 200 nm and 50 nm respectively) and **(B)** Liquid tapping AFM (Scale bar: 270 nm and 100 nm respectively). The microscopy images of Cu$^+$-Nap-FFMTCGGCR^{ag} (100 µM, Milli-Q) observed under **(C)** Cryo-EM (Scale bar: 200 nm and 50 nm respectively) and **(D)** Liquid tapping AFM (Scale bar: 600 nm and 280 nm respectively). **(E)** CD spectra of Nap-FFMTCGGCR^{ag} (100 µM) and Cu$^+$-Nap-FFMTCGGCR^{ag} (1:1, 100 µM). **(F)** The Ellman's reagent assay showing 80% reduction in the surface thiols of Nap-FFMTCGGCR^{ag} (100 µM) after adding 1 mol. equivalent of Cu$^+$. G) The binding titration curve of Nap-FFMTCGGCR^{ag} (100 µM) and Bca (100 µM) towards Cu$^+$ (0–160 µM). The data represented as mean±s.d., $n=3$. The diameter of individual fibers was obtained from TEM images measured using Image J data processing software. The data represented as mean±s.d., $n=100$. The helical length was obtained from AFM images measured using NanoScope Analysis data processing software. The data represented as mean±s.d., $n=5$.

ure 3E). These observations suggest that the morphology of **Nap-FFMTCGGCR**^{ag} nanofibers did not alter after binding to Cu$^+$.[42,43] Ellman's reagent assay showed 80 % decrease in the free thiols of the **Nap-FFMTCGGCR**^{ag} upon binding to 1 mol. equivalent Cu$^+$ (Figure 3F, Figure S21). The surface charge distribution of **Nap-FFMTCGGCR**^{ag} showed an average zeta potential of 46 ± 2.2 mV (100 µM), which remained unchanged (46.9 ± 2 mV, Figure S22) after Cu$^+$ binding (1:1). A 1:1 binding stoichiometry of **Nap-FFMTCGGCR**^{ag} to Cu$^+$ was observed in a titration experiment using the known Cu$^+$ chelator bicinchoninate (Bca) (Figure S23).[44] Bca binds Cu$^+$ with a 2:1 (Bca:Cu$^+$) stoichiometric ratio forming a pink-colored complex of $[Cu^+(Bca)_2]^{3-}$ that absorbs at 562 nm. Titration of Cu$^+$ (0–160 µM) and 100 µM of Bca showed a linear increase in the absorbance at 562 nm reaching a maximum upon the addition of ~0.5 equivalent (50 µM) of Cu$^+$ corresponding to the formation of $[Cu^+(Bca)_2]^{3-}$. However, the similar titration into the solution containing the mixture of Bca (100 µM) and **Nap-FFMTCGGCR**^{ag} (100 µM) showed a delayed increase in the absorbance at 562 nm, requiring ~140 µM of Cu$^+$ to reach the plateau (Figure 3G). The titration curve indicates that the **Nap-FFMTCGGCR**^{ag} binds Cu$^+$ with a stoichiometry of nearly 1:1. Additionally, these results indicate that **Nap-FFMTCGGCR**^{ag} binds Cu$^+$ even in the presence of Bca. Bca binds Cu$^+$ with a high dissociation constant of $10^{-17.3}$ M as reported previously,[44,45] which allowed us to estimate the dissociation constant of **Nap-FFMTCGGCR**^{ag} with bound Cu$^+$ in a competitive binding titration experiment with Bca. A very low K_D of $(2.3 \pm 1.6) \times 10^{-14.3}$ M[44] was observed for **Nap-FFMTCGGCR**^{ag} with Cu$^+$ (Table S2), which is ~100-fold lower than the K_D of **Cu$^+$-Nap-FFMTCGGCR**^{mn}. The K_D of **Cu^I-Nap-FFMTCGGCR**^{mn} complex is about $(3.03 \pm 1.27) \times 10^{-12.3}$ M (Table S3).

Next, we examined the effect of glutathione (GSH) on the Cu$^+$ binding ability and self-assembly of **Nap-FFMTCGGCR**^{ag}. The Cu$^+$ binding titration (0–160 µM) against Bca in the presence of GSH (100 µM) did not significantly change the titration curve, indicating that GSH is not a competitor of Bca for Cu$^+$ at this concentration. However, a similar titration of Cu$^+$ into a solution containing Bca (100 µM), GSH (100 µM) and **Nap-FFMTCGGCR**^{ag} (100 µM) showed a delayed increase in the absorbance at 562 nm, requiring ~140 µM of Cu$^+$ to reach the plateau (Figure S24A). This suggests that the 1:1 stoichiometric binding of **Nap-FFMTCGGCR**^{ag} to Cu$^+$ is conserved in the presence of GSH. We also analyzed whether fibrils can be formed in the presence of intracellularly relevant concentrations of GSH (0.1 to 5 mM) (Figure S24B). TEM images of the **Nap-FFMTCGGCR**^{ag} prepared in Milli-Q water containing GSH revealed the presence of fibrils. Additionally, the pre-assembled **Nap-FFMTCGGCR**^{ag} exhibited high stability when incubated with varying concentrations of GSH, as analyzed by the TEM images and count rate (kcps) measurement analysis which remained unaffected for up to 48 h (Figure S24C–D).

Intracellular Self-assembly of Nap-FFMTCGGCR

Triple negative MDA-MB-231 breast cancer cells have a high demand for Cu$^+$ compared to healthy cells.[46,47] To image the internalization and intracellular self-assembly of **Nap-FFMTCGGCR** in MDA-MB-231 cells by fluorescence microscopy, the fluorescent peptide derivative **NBD-FFMTCGGCR** was synthesized by replacing naphthalene with 4-nitro-2,1,3-benzoxadiazole (NBD) (Figure S25). The NBD fluorophore has been used before for imaging *in cellulo* self-assembled nanofibers (Figure 4A).[48] **NBD-FFMTCGGCR** and **Nap-FFMTCGGCR** co-assemble into nanofibers with an average diameter of 12.5 ± 0.7 nm (Figure S26). These co-assembled fibers absorb light at 400–500 nm and emit at 500–700 nm as depicted in Figure S27, rendering them suitable for visualization under confocal microscopy. Notably, **NBD-FFMTCGGCR** itself does not self-assemble into nanofibers at 100 µM (Figure S28). The MDA-MB-231 cells were incubated with a mixture of **NBD-FFMTCGGCR** and **Nap-FFMTCGGCR** (5 µM each, 10 µM total), which forms co-aggregates inside the cells, and were visualized by confocal microscopy after 24 h. A bright green fluorescence was observed from the cell confirming cellular internalization (Figure 4B) and intracellular nanofiber formation of **Nap/NBD-FFMTCGGCR**^{ag} via co-assembly as shown in Figure 4A. In contrast, **NBD-FFMTCGGCR** (10 µM) did not form any aggregates inside cells, most likely due to the higher CAC of NBD versus Nap (Figure 4C).[49]

The CAC of **NBD-FFMTCGGCR** was determined to be 105 µM using Nile red assay, whereas the CAC of **Nap/NBD-FFMTCGGCR** was 68.7 µM. The lower CAC of **Nap/NBD-FFMTCGGCR** was attributed to the higher self-assembling propensity of **Nap-FFMTCGGCR** (CAC: 50 µM) compared to **NBD-FFMTCGGCR**. **NBD-FFMTCGGCR** showed the formation of fibers (average diameter was 11.9 ± 0.3 nm) when analyzed at 200 µM (Milli-Q water). The fluorescence emission spectra analysis of both **NBD-FFMTCGGCR** and **Nap/NBD-FFMTCGGCR** exhibited a concentration ([c]) dependent increase in the fluorescence emission. A plot of Log[c] versus I_{max} (maximum intensity of emission) at 546 nm showed a slow increment below the CAC, and an exponential increment above the CAC, in both cases (Figure S29). This indicates that the self-assembly enhances the emission of **NBD-FFMTCGGCR**^{ag}. Therefore, the observed fluorescence from the cell upon the incubation of **Nap/NBD-FFMTCGGCR** indicates the formation of **Nap/NBD-FFMTCGGCR**^{ag} within the cell, which can be easily achieved upon co-incubation. A quantitative analysis revealed a cellular uptake of 0.192 ± 0.003, 0.206 ± 0.006 and 0.253 ± 0.006 µM of **NBD-FFMTCGGCR** (per 500 k cells) when incubated with 5, 10, and 20 µM of **Nap/NBD-FFMTCGGCR**, respectively, indicating a concentration dependent uptake of **NBD-FFMTCGGCR** inside cancer cells (Figure S30).

Next, holotomographic microscopy was applied to study the label-free assembly of **Nap-FFMTCGGCR** inside the cell. Holotomographic microscopy measures the refractive indices of the cellular compartments to create a holotomo-
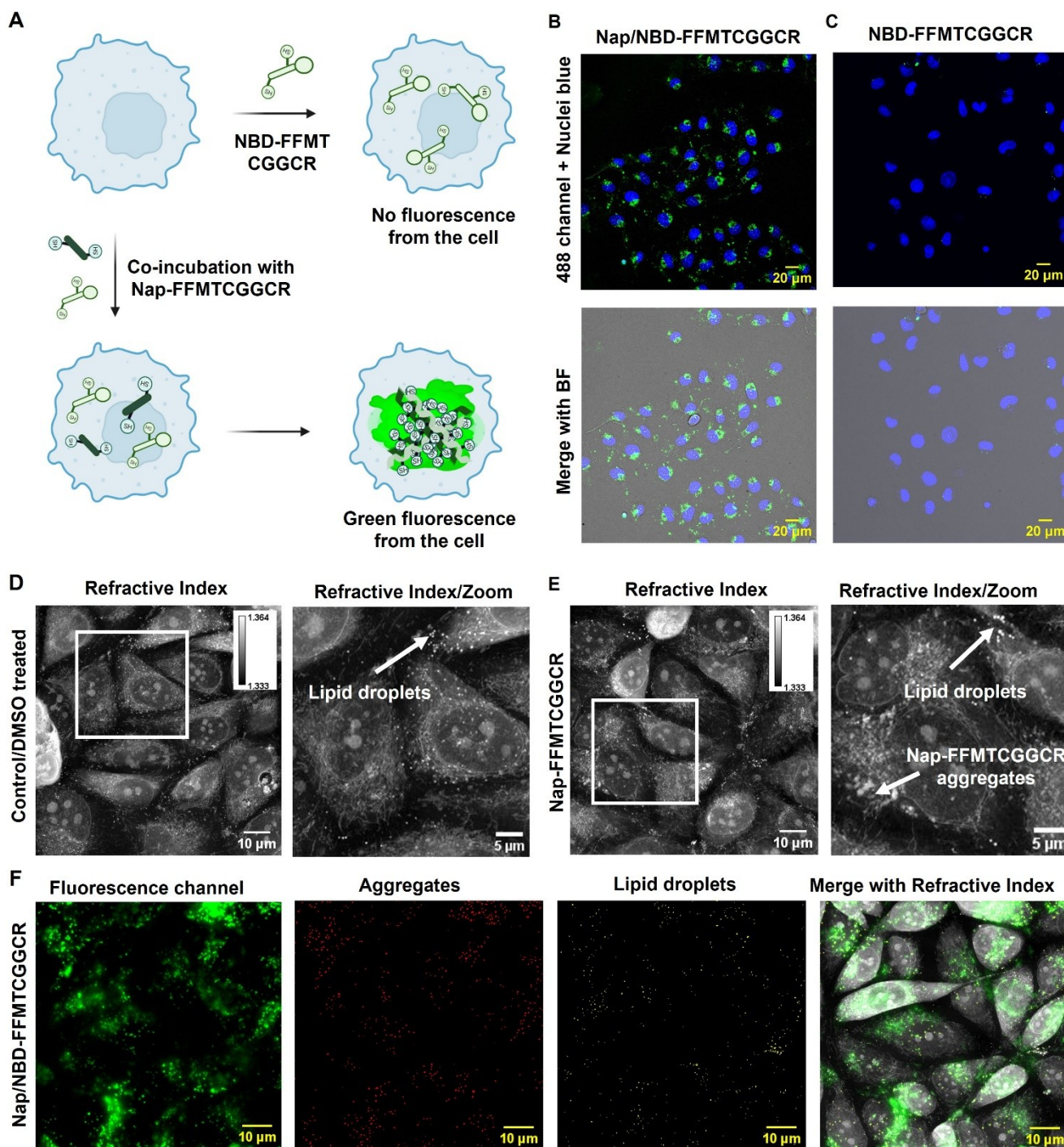
Figure 4. **(A)** Schematic illustration of co-assembly approach to study the self-assembly of Nap-FFMTCGGCR inside the cell. Confocal microscopy images of MDA-MB-231 cells treated with **(B)** NBD/Nap-FFMTCGGCR(10 μM) and **(C)** NBD-FFMTCGGCR(10 μM) imaged after 24 h of incubation. The nuclei were labelled with NucBlue™. Holotomogram of **(D)** control (treated with DMSO) MDA-MB-231 cells. The calibration bar indicates the refractive index (RI). The lipid droplets are marked with arrows, and **(E)** MDA-MB-231 cells treated with Nap-FFMTCGGCRimaged after 24 h showing the presence of aggregates of RI ~1.357 ± 0.004. **(F)** The segmented holotomogram of MDA-MB-231 treated with Nap/NBD-FFMTCGGCRshowing the appearance of green fluorescence corresponding to the aggregates. The yellow dots indicate lipid droplets and red dots indicate aggregates formed inside the cell upon treatment with Nap/NBD-FFMTCGGCR. The segmentation was performed using random forest-based pixel classification.

gram. The peptides that aggregated or self-assembled into nanofibers possess refractive indices (~1.35–1.36) measurable by a holotomography. First, the holotomogram of untreated MDA-MB-231 cells was taken as shown in Figure 4D. The refractive indices of the cellular components such as nucleoli, lipid droplets and mitochondria were

measured approximately as 1.349 ± 0.0043, 1.366 ± 0.0016 and 1.342 ± 0.0014, respectively (in DMEM medium). Incubating MDA-MB-231 cells with **Nap-FFMTCGGCR** (10 or 20 μM) showed the presence of aggregates inside the cell possessing a refractive index of 1.357 ± 0.004 (Figure 4E, Figure S31), which can be visually distinguished from lipid droplets.

To differentiate the **Nap-FFMTCGGCR**[ag] from lipid droplets within the cell using fluorescence, **Nap/NBD-FFMTCGGCR** were co-assembled inside the cells. **NBD-FFMTCGGCR** (10 μM) itself does not form aggregates in cells and therefore, no fluorescence signals were observed under holotomography as depicted in Figure S32A, which is consistent with the confocal images. However, after incubation of both **Nap/NBD-FFMTCGGCR** (10 μM), intracellular aggregates were detected by their green fluorescence suggesting that co-incubation results in the formation of **Nap/NBD-FFMTCGGCR**[ag] inside the cell (Figure S32B). Notably, 10 μM of **Nap/NBD-FFMTCGGCR** does not self-assemble into nanofibers in cell-free tests, underscoring the significance of intracellular enrichment of both peptides to self-assemble into structures inside the cell when incubated at 10 μM (Figure S33). We have performed the segmentation of **Nap/NBD-FFMTCGGCR**[ag] and lipid droplets as shown in Figure 4F. The lipid droplets were present in the untreated control cells, as well as in the **NBD-FFMTCGGCR** and **Nap/NBD-FFMTCGGCR** treated cells while peptide aggregates were present only in **Nap/NBD-FFMTCGGCR** treated cells (Figure 4F, Figure S34). The lipid droplets and aggregates showed no co-localization (Figure S35). To verify whether the co-assembled structures were localized in any subcellular compartment, cellular co-localization analysis was conducted. MDA-MB-231 cells were incubated with **Nap/NBD-FFMTCGGCR** (10 μM) for 12 h before imaging by confocal microscopy. No co-localization was found with mitochondria (MitoTracker™ Red FM) or with the endoplasmic reticulum (ER-Tracker™ Red). Partial co-localization with endo-lysosomes (Lyso-Tracker™ Red) (Pearson coefficient 0.31) suggests that the peptides likely internalize via endocytosis (Figure S36–S38).

Nap-FFMTCGGCR Induces Cancer Cell Apoptosis

Due to the heightened demand of Cu^+ metabolism for the growth and proliferation of breast cancer cells, we envisaged that intracellular Cu^+ binding of **Nap-FFMTCGGCR** might cause adverse effects on these cells.[50,51] To get insight into this speculation, at first, we examined the survival rate of MDA-MB-231 breast cancer cells after treating them with **Nap-FFMTCGGCR** in a time-dependent manner. MDA-MB-231 cells were incubated with 10 μM of **Nap-FFMTCGGCR** to analyze the cell survival over time. At first, we examined the survival rate of MDA-MB-231 breast cancer cells after treating them with **Nap-FFMTCGGCR** in a time-dependent manner. MDA-MB-231 cells were incubated with 10 μM of **Nap-FFMTCGGCR** to analyze the cell survival over time. For an incubation time of 24 h with **Nap-FFMTCGGCR**, $78.8 \pm 8.8\%$ viable cells were detected.

After 48 and 72 h, the cell survival rate was further reduced to $39.2 \pm 4.5\%$ and $14.2 \pm 2.9\%$, respectively, suggesting that treatment with **Nap-FFMTCGGCR** effectively reduced the viability of MDA-MB-231 breast cancer cells over time (Figure 5A).

However, the observed reduction in cell viability could either originate from **Nap-FFMTCGGCR**[ag] formed inside the cell or from a synergistic effect arising from both aggregation and the disruption of Cu^+ homeostasis. Therefore, the control peptide, **Nap-FFMTGGR**, that also self-assembles (CAC: 45 μM in Milli-Q water) but does not bind Cu^+ due to the absence of the cysteine residues was synthesized (Figure S40–41). First, fiber formation of **Nap-FFMTGGR**[ag] was assessed outside cells and fibers with diameter 5.9 ± 0.3 nm were obtained (Figure S42). Next, the impact of *in cellulo* aggregation of **Nap-FFMTGGR** (10 μM incubation) on the cell viability was tested. However, cells remained viable even after 48 h, and only after 72 h, the cell viability decreased to $55.7 \pm 2.9\%$ (Figure 5B). This observation suggests, the peptide aggregates, devoid of Cu^+-binding motif required significantly longer incubation time to induce cytotoxic effects on MDA-MB-231 cells. Concentration-dependent cell viability analysis of both **Nap-FFMTCGGCR** and **Nap-FFMTGGR** was performed on MDA-MB-231 cells (48 h incubation) showed that **Nap-FFMTCGGCR** induced cytotoxicity with an IC_{50} of 6.5 μM while **Nap-FFMTGGR** showed an approximate 3-fold higher IC_{50} of 19.9 μM (Figure 5C). Interestingly, both compounds did not exhibit any cytotoxicity in normal HEK 293 T cells at the tested conditions (48 h, up to 20 μM) indicating pronounced cytotoxicity in cancer versus healthy cells (Figure 5D).

The observed non-toxicity of **Nap-FFMTCGGCR** in HEK 293T cells under the tested conditions were primarily attributed to a lower (~1.4-fold) cellular uptake of **Nap-FFMTCGGCR** in **HEK 293T** compared to **MDA-MB 231**, most likely owing to the higher negative surface charge of cancer cells (Figure S43–S44).[52] The apoptosis assay monitored by FITC-Annexin V and propidium iodide (PI) showed Annexin V staining on the plasma membrane of the MDA-MB-231 cells treated by **Nap-FFMTCGGCR**, indicating that the cells initiated early apoptotic pathways after 48 h (10 μM) of incubation (Figure 5E). Notably, the absence of PI signal indicates that cell death was primarily caused by apoptosis. In contrast, **Nap-FFMTGGR** did not induce apoptosis under this condition 48 h (10 μM) (Figure 5F).

Nap-FFMTCGGCR Interrupt Cu^+ Homeostasis and Induces Oxidative Stress to Cancer Cells

Next, we investigated the underlying mechanisms leading to the cell toxicity upon treatment with **Nap-FFMTCGGCR**. We assume that the high affinity of **Nap-FFMTCGGCR**[ag] towards Cu^+ possibly enables them to successfully compete with cytosolic Cu^+ chaperones or intracellular Cu^+-complexes. Cu^+ homeostasis is strongly correlated with the redox balance of the cell because SOD1, the key enzyme responsible for the redox balance of the cell, uses Cu^+ as the
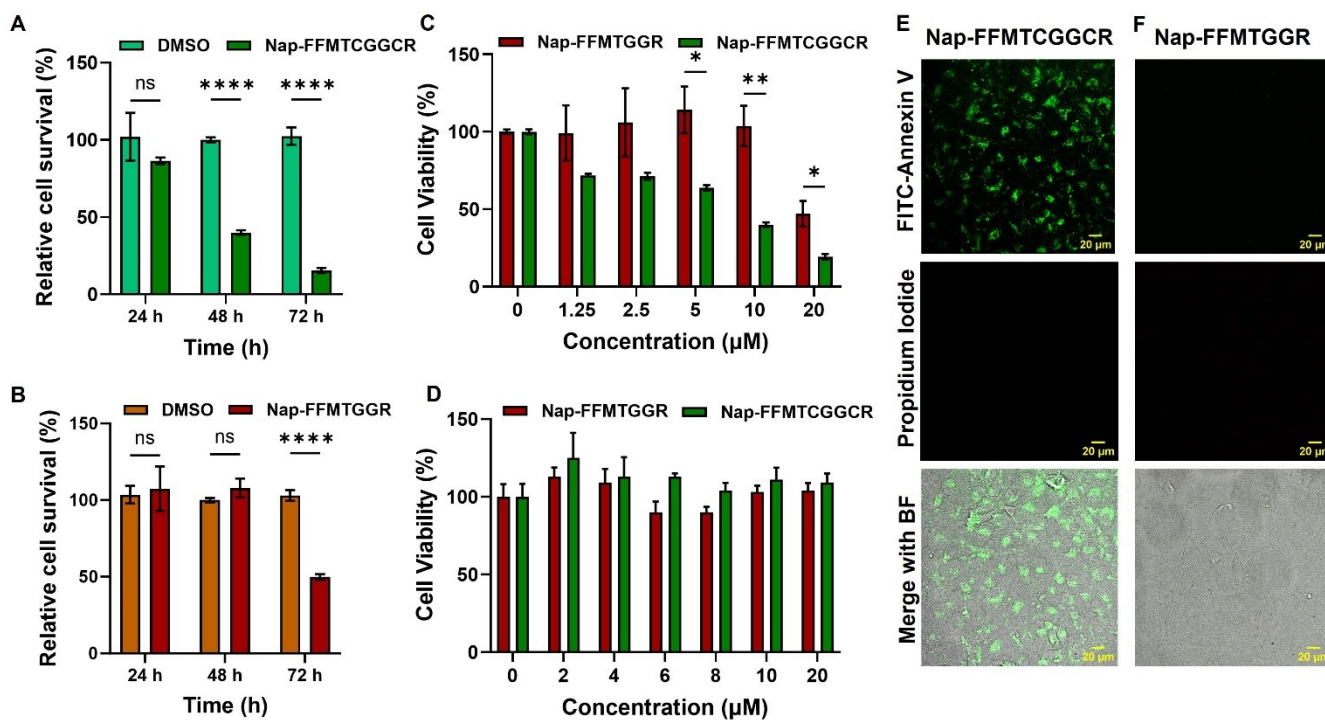
Figure 5. The response of MDA-MB-231 cells towards the treatment with **(A)** Nap-FFMTCGGCR (10 μM) and **(B)** Nap-FFMTGGR (10 μM) over time. Dose-dependent cell viability analysis of Nap-FFMTCGGCR and Nap-FFMTGGR towards **(C)** MDA-MB-231 cells and **(D)** HEK 239T cells analyzed after 48 h. Live/dead cell assay performed using FITC-Annexin V/Propidium Iodide staining after treating with **(E)** Nap-FFMTCGGCR (10 μM, 48 h) and **(F)** Nap-FFMTGGR (10 μM, 48 h). Statistical analysis was performed using unpaired t-test corrected for Bonferroni-Dunn method, set P value threshold 0.05, 0.1234 (ns), **P < 0.0332, **P < 0.0021, ***P < 0.0002, ****P < 0.0001)). The data represented as mean ± s.d., $n = 3$.

cofactor.[53] SOD1 is an antioxidant enzyme that scavenges the superoxide anion by converting the free radical to oxygen and hydrogen peroxide.[54,55] We postulates that the Cu^+ binding ability of **Nap-FFMTCGGCR**[ag] could induce Cu^+ starvation of SOD1 enzyme, causing redox imbalance within the cell. First, we studied whether the SOD1 activity of the cells was affected upon treatment with **Nap-FFMTCGGCR**. The cellular SOD1 activity of the untreated control cell group was measured as 0.404 ± 0.01 U/mL. After treating with **Nap-FFMTCGGCR** for 48 h (20 μM), there was 8-fold reduction in activity (0.05 ± 0.003 U/mL). In contrast, treatment with **Nap-FFMTGGR** showed no noticeable changes (0.43 ± 0.02 U/mL) relative to the untreated control group (Figure 6A, Figure S45). We anticipate that **Nap-FFMTCGGCR**[ag] formed within the cell could potentially interact with CCS chaperone, thereby interrupting the delivery of Cu^+ to SOD1. SOD1 is the counter chaperone for CCS. Given that Cu^+ serves as a cofactor for the proper functioning of SOD1, inadequate Cu^+ likely leads to a loss of SOD1 activity.

Subsequently, we explored whether the reduced SOD1 activity contributes to elevated cellular oxidative stress level using an assay based on 2',7'-dichlorofluorescin diacetate (DCFDA) probe. DCFDA is a cell-permeable fluorogenic dye that measures the activity of reactive oxygen species (ROS) such as hydroxyl, peroxyl and singlet oxygen within the cell. MDA-MB-231 cells were treated with 20 μM of **Nap-FFMTCGGCR** or **Nap-FFMTGGR** for 48 h. Following confocal imaging analysis after staining with the DCFDA probe, bright fluorescence was observed from the cells treated with **Nap-FFMTCGGCR** (Figure 6B). However, **Nap-FFMTGGR** treated cells did not show fluorescence within the tested conditions (20 μM, 48 h). This observation was further validated by flow cytometric analysis (Figure S46). We anticipate that the elevated cellular oxidative stress can induce metabolic defects in cells. To examine whether intracellular aggregation and consequent Cu^+ binding of **Nap-FFMTCGGCR**[ag] induce any metabolic defects, we evaluated cellular ATP levels following treatment with **Nap-FFMTCGGCR** or **Nap-FFMTGGR**. The ATP concentration of the untreated control MDA-MB-231 cell group was measured as 1.8 ± 0.006 μM. As anticipated, treatment with **Nap-FFMTCGGCR** (20 μM, 48 h) reduced the ATP level to 0.74 ± 0.09 μM. However, the ATP level in the **Nap-FFMTGGR** treated group showed no significant difference (1.68 ± 0.04 μM) compared to the control group under similar conditions (Figure 6C, Figure S47).

Fiber Morphology is Essential to Interrupt Intracellular Cu^+ Homeostasis

To investigate the influence of fiber morphology on the disruption of intracellular Cu^+ homeostasis, we conducted
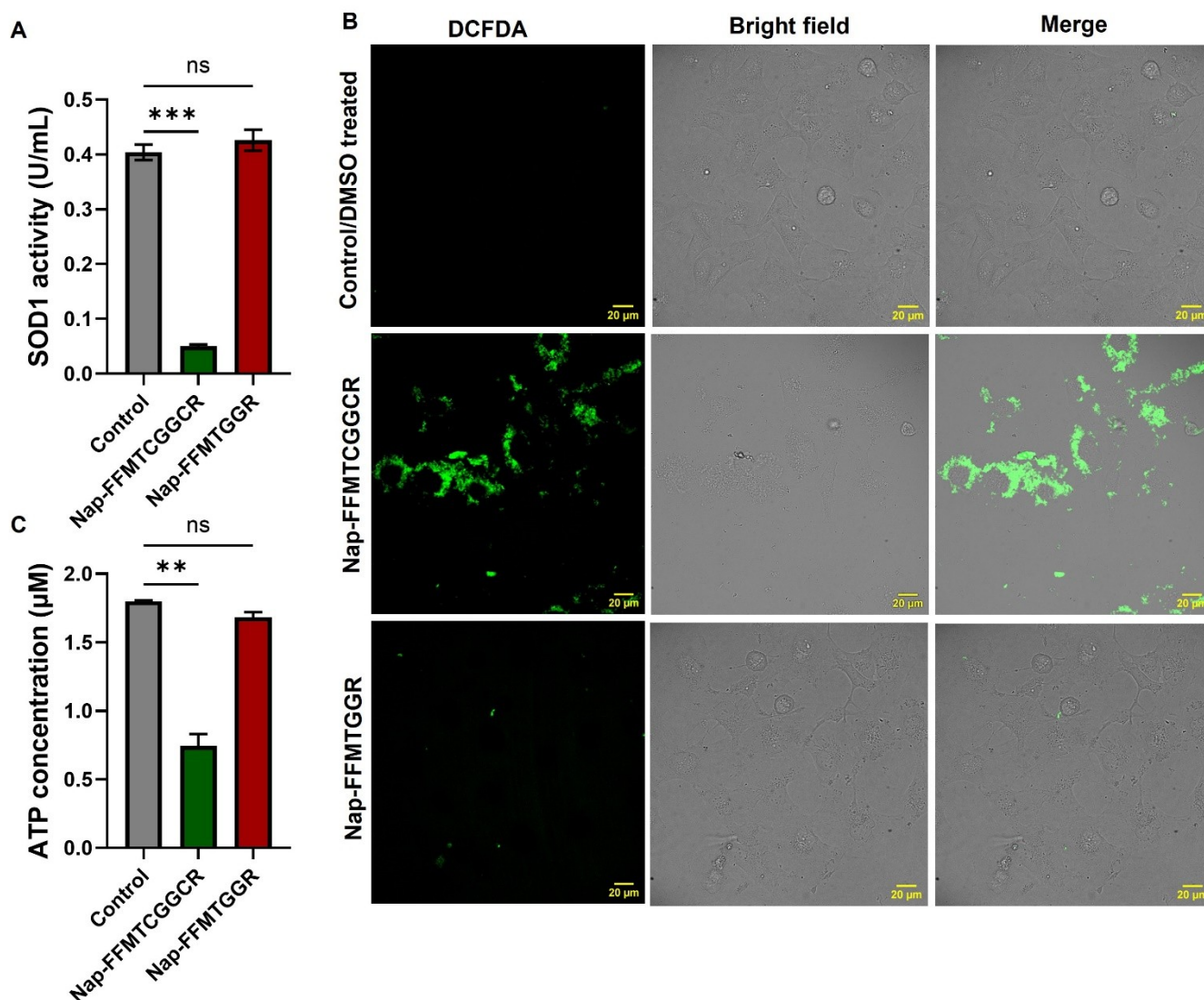
Figure 6. (A) SOD1 analysis of MDA-MB-231 cells after treating with Nap-FFMTCGGCR or Nap-FFMTGGR (20 µM, 48 h). (B) ROS generation inside the MDA-MB-231 cells measured using DCFDA probe after treating with Nap-FFMTCGGCR or Nap-FFMTGGR (20 µM, 48 h), (C) ATP concentration of MDA-MB-231 cells after treating with Nap-FFMTCGGCR or Nap-FFMTCGGCR (20 µM, 48 h). The error bars represent standard deviation from three replicate sample measurements. Statistical analysis was performed using one-way ANOVA (corrected for Bonferroni method). P values: 0.12 (ns), 0.033 (*), 0.002 (**), < 0.001 (***). The data represented as mean ± s.d., $n = 3$.

experiments involving a control peptide, **Nap-MTCGGCR** (Figure S48).

Nap-MTCGGCR incorporates a Cu^+-binding domain without a self-assembly promoter (**Nap-FF**). The Cu^+ binding of **Nap-MTCGGCR** was validated through UV/Vis spectral analysis, revealing the increase in the absorbance at 254–300 nm upon binding to Cu^+ (Figure 7A). **Nap-MTCGGCR** showed no self-assembled structures in the TEM when analyzed at 100 µM (Figure 7B, Figure S49). The cytotoxicity analysis performed on MDA-MB-231 cells revealed no adverse effects even at a treatment concentration of 100 µM tested for 72 h. This result suggests that the presence of the Cu^+-binding domain at the molecular level alone is insufficient to disrupt the Cu^+ homeostasis within the cellular environment. In support, the Annexin V/

PI staining assay did not exhibit positive staining for either Annexin V or PI following treatment with **Nap-MTCGGCR** (20 µM, 46 h), indicating that **Nap-MTCGGCR** failed to trigger the cell death in MDA-MB-231 cells (Figure S50). These outcomes underscore the significance of intracellular self-assembly in effectively binding and disrupting cellular Cu^+ homeostasis.

Conclusions

While targeting Cu^+ homeostasis has emerged as a promising approach for cancer therapeutics, progress in this field has been limited by the insufficient disruption of Cu^+ homeostasis by small molecules. Inspired by natural Cu^+
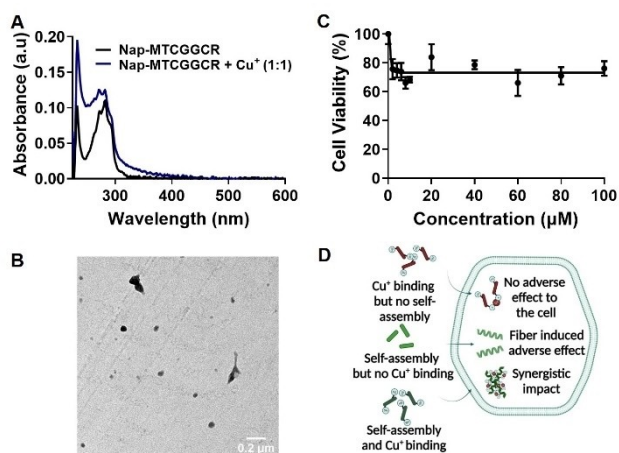
Figure 7. (A) The UV/Vis spectra of Nap-MTCGGCR (40 µM, Milli-Q) in response to the addition of Cu⁺ (1 mol. equivalent). (B) TEM image of Nap-MTCGGCR (100 µM) showing no nanostructure formation. (C) Cell viability analysis of Nap-MTCGGCR against MDA-MB-231 cells tested for 72 h. (D) Schematic illustration of the behavior of Nap-MTCGGCR, Nap-FFMTGGR and Nap-FFMTCGGCR inside a cancer cell. The data represented as mean ± s.d., $n = 3$ for C.

chaperones, we amplify the capabilities of Cu⁺-binding motifs using supramolecular concepts to localize a high local concentration of Cu⁺-binding domain onto self-assembled nanostructures within cells. These **Nap-FFMTCGGCR**[ag] structures successfully compete with the natural Cu⁺ binding systems in triple negative breast cancer cells (MDA-MB-231), addressing the limitation possessed by small molecules in interrupting Cu⁺ homeostasis. We were able to dissect the cellular responses due to Cu⁺ binding from those initiated exclusively though fibril formation based on the control peptide **Nap-FFMTGGR** that assembles but does not bind Cu⁺. Moreover, we substantiated that the mere existence of the Cu⁺-binding motif does not ensure the interruption of Cu⁺ homeostasis within the cell, as evidenced by the analysis of a non-assembling control peptide, **Nap-MTCGGCR**. We show that molecular functions combined with *in situ* self-assembly technologies is an attractive strategy to amplify their bioactivity in living cells.

Supporting Information

The authors have cited additional references within the Supporting Information.[44,56–61]

Acknowledgements

Conflict of Interest

The authors declare no conflict of interest.

Data Availability Statement

The data that support the findings of this study are available in the supplementary material of this article.

[1] Y. Liu, Y. Wang, S. Song, H. Zhang, *Chem. Sci.* **2021**, *12*, 12234–12247.

[2] M. Drążkiewicz, E. Skórzyńska-Polit, Z. Krupa, *BioMetals* **2004**, *17*, 379–387.

[3] L. M. Ruiz, A. Libedinsky, A. A. Elorza, *Front. Mol. Biosci.* **2021**, *8*, 711227.

[4] A. Dancis, D. S. Yuan, D. Haile, C. Askwith, D. Eide, C. Moehle, J. Kaplan, R. D. Klausner, *Cell* **1994**, *76*, 393–402.

[5] J. Wang, C. Luo, C. Shan, Q. You, J. Lu, S. Elf, Y. Zhou, Y. Wen, J. L. Vinkenborg, J. Fan, H. Kang, R. Lin, D. Han, Y. Xie, J. Karpus, S. Chen, S. Ouyang, C. Luan, N. Zhang, H. Ding, M. Merkx, H. Liu, J. Chen, H. Jiang, C. He, *Nat. Chem.* **2015**, *7*, 968–979.

[6] A. Gupte, R. J. Mumper, *Cancer Treat. Rev.* **2009**, *35*, 32–46.

[7] X. Chen, Q. Cai, R. Liang, D. Zhang, X. Liu, M. Zhang, Y. Xiong, M. Xu, Q. Liu, P. Li, P. Yu, A. Shi, *Cell Death Dis.* **2023**, *14:105*, 1–12.

[8] V. C. Shanbhag, N. Gudekar, K. Jasmer, C. Papageorgiou, K. Singh, M. J. Petris, *Biochim. Biophys. Acta* **2021**, *1868*, 118893.

[9] P. Lelièvre, L. Sancey, J. L. Coll, A. Deniaud, B. Busser, *Cancers* **2020**, *12*, 1–25.

[10] B. E. Kim, T. Nevitt, D. J. Thiele, *Nat. Chem. Biol.* **2008**, *4*, 176–185.

[11] W. J. Chen, H. T. Wu, C. L. Li, Y. K. Lin, Z. X. Fang, W. T. Lin, J. Liu, *Front. Cell Dev. Biol.* **2021**, *9*, 752426.

[12] J. F. Eisses, J. H. Kaplan, *J. Biol. Chem.* **2005**, *280*, 37159–37168.

[13] M. L. Turski, D. J. Thiele, *J. Biol. Chem.* **2009**, *284*, 717–72.

[14] G. F. Chen, V. Sudhahar, S. W. Youn, A. Das, J. Cho, T. Kamiya, N. Urao, R. D. McKinney, B. Surenkhuu, T. Hamaku-bo, H. Iwanari, S. Li, J. W. Christman, S. Shantikumar, G. D. Angelini, C. Emanueli, M. U. Fukai, T. Fukai, *Sci. Rep.* **2025**, *5*, 14780.

[15] L. Banci, I. Bertini, S. Ciofi-Baffoni, T. Kozyreva, K. Zovo, P. Palumaa, *Nature* **2010**, *465*, 645–648.

[16] A. Lasorsa, M. I. Nardella, A Rosato, V. Mirabelli, R. Caliandro, R. Caliandro, G. Natile, F. Arnesano, *J. Am. Chem. Soc.* **2019**, *141*, 12109–12120.

[17] S. C. Dodani, S. C. Leary, P. A. Cobine, D. R. Winge, C. J. Chang, *J. Am. Chem. Soc.* **2011**, *133*, 8606–8616.

[18] Y. Hatori, S. Inouye, R. Akagi, *IUBMB Life* **2017**, *69*(4), 246–254.

[19] J. T. Rubino, M. P. Chenkin, M. Keller, P. Riggs-Gelasco, K. J. Franz, *Metallomics* **2011**, *3*, 61–73.

[20] A. Gupte, R. J. Mumper, *Cancer Treat. Rev.* **2009**, *35*, 32–46.

[21] G. M. Yang, L. Xu, R. M. Wang, X. Tao, Z. W. Zheng, S. Chang, D. Ma, C. Zhao, Y. Dong, S. Wu, J. Guo, Z. Y. Wu, *Cell Rep.* **2023**, *42*, 112417.

[22] E. D. Harris, M. C. M. Reddy, S. Majumdar, M. Cantera, *BioMetals* **2003**, *16*, 55–61.

[23] S. Baldari, G. D. Rocco, G. Toietta, *Int. J. Mol. Sci.* **2020**, *21*, 1069.

[24] S. K. Gupta, V. K. Shukla, M. P. Vaidya, S. K. Roy, S. Gupta, *J. Surg. Oncol.* **1993**, *52*, 172–175.

[25] X. Zhang, Q. Yang, *Int. J. Med. Res.* **2018**, *46*, 4863–4873.

[26] J. T. Dabek, M. Harkonen, H. Adlercreutz, M. Hyvönen-Dabek, *Nutr. Cancer* **1992**, *17*, 195–201.

[27] L. Turecky`, P. Kalina, E. Uhlíková, Ŝ. Námerová, J. Križko, *Klin. Wochenschr.* **1984**, *62*, 187–189.

[28] A. P. Fang, P. Y. Chen, X. Y. Wang, Z. Y. Liu, D. M. Zhang, Y. Luo, G. C. Liao, J. A. Long, R. H. Zhong, Z. G. Zhou, Y. J. Xu, X. J. Xu, W. H. Ling, M. S. Chen, Y. J. Zhang, H. L. Zhu, *Int. J. Cancer* **2019**, *144*, 2823–2832.

[29] E. J. Ge, A. I. Bush, A. Casini, P. A. Cobine, J. R. Cross, G. M. DeNicola, Q. P. Dou, K. J. Kranz, V. M. Gohil, S. Gupta, S. G. Kaler, S. Lutsenko, V. Mittal, M. J. Petris, R. Polishchuk, M. Ralle, M. L. Schilsky, N. K. Tonks, L. T. Vahdat, L. V. Aelst, D. Xi, P. Yuan, D. C. Brady, C. J. Chang, *Nat. Rev. Cancer* **2022**, *22*, 102–113.

[30] A. K. Boal, A. C. Rosenzweig, *Chem. Rev.* **2009**, *109*, 4760–4779.

[31] P. Rousselot-Pailley, O. Sénèque, C. Lebrun, S. Crouzy, D. Boturyn, P. Dumy, M. Ferrand, P. Delangle, *Inorg. Chem.* **2006**, *45*, 5510–5520.

[32] Z. Feng, H. Wang, F. Wang, Y. Oh, C. Berciu, Q. Cui, E. H. Egelman, B. Xu, *Cell Rep. Phys. Sci.* **2020**, *1*, 100085.

[33] H. Wang, Z. Feng, B. Xu, *Chem. Soc. Rev.* **2017**, *46*, 2421.

[34] W. Tan, Q. Zhang, J. Wang, M. Yi, Hongjian He, B. Xu, *Angew. Chem. Int. ed.* **2021**, *60*, 12796–12801 <

[35] X. Liu, M. Li, J. Liu, Y. Song, B. Hu, C. Wu, A. A. Liu, H. Zhou, J. Long, L. Shi, Z. Yu, *J. Am. Chem. Soc.* **2022**, *144*, 9312–9323.

[36] X. Liu, F. Tian, Z. Zhang, J. Liu, S. Wang, R. C. Guo, B. Hu, H. Wang, H. Zhu, A. A. Liu, L. Shi, Z. Yu, *J. Am. Chem. Soc.* **2024**, *146*, 24177–24187.

[37] R. C. Guo, N. Wang, W. Wang, Z. Zhang, W. Luo, Y. Wang, H. Du, Y. Xu, G. Li, Z. Yu, *Angew. Chem. Int. Ed.* **2023**, *62*, e202314578.

[38] K. M. Davies, J. F. B. Mercer, N. Chen, K. L. Double, *Clin. Sci.* **2016**, *130*, 565–574.

[39] L. Cui, A. M. Gouw, E. L. LaGory, S. Guo, N. Attarwala, Y. Tang, J. Qi, Y. S. Chen, Z. Gao, K. M. Casey, A. A. Bazhin, M. Chen, L. Hu, J. Xie, M. Fang, C. Zhang, Q. Zhu, Z. Wang, A. J. Giaccia, S. S. Gambhir, W. Zhu, D. W. Felsher, M. D. Pegram, E. A. Goun, A. Le, J. Rao, *Nat. Biotechnol.* **2021**, *39*, 357–367.

[40] P. Roth, R. Meyer, I. Harley, K. Landfester, I. Lieberwirth, M. Wagner, D. Y. W. Ng, T. Weil, *Nat. Synth.* **2023**, *2*, 980–988.

[41] A. Rigo, A. Corazza, M. L. Paolo, M. Rossetto, R. Ugolini, M. Scarpa, *J. Inorg. Biochem.* **2004**, *98*, 1495–1501.

[42] R. C. Hider, G. Kupryszewski, P. Rekowski, B. Lammek, *Biophys. Chem.* **1988**, *31*, 45–51.

[43] V. Joshi, T. Shivach, N. Yadav, A. S. Rathore, *Anal. Chem.* **2014**, *86*, 11606–11613.

[44] Z. Xiao, J. Brose, S. Schimo, S. M. Ackland, S. L. Fontaine, A. G. Wedd, *J. Biol. Chem.* **2011**, *286*, 11047–11055.

[45] J. Bros, S. L. Fontaine, A. G. Wedd, Z. Xiao, *Metallomics* **2014**, *6*, 793–808.

[46] O. Karginova, C. M. Weekley, A. Raoul, A. Alsayed, T. Wu, S. S. Y. Lee, C. He, O. I. Olopade, *Mol. Cancer Ther.* **2019**, *18* (5), 873–885.

[47] D. Ramchandani, M. Berisa, D. A. Tavarez, Z. Li, M. Miele, Y. Bai, S. B. Lee, Y. Ban, N. Dephoure, R. C. Hendrickson, S. M. Cloonan, D. Gao, J. R. Cross, L. T. Vahdat, V. Mittal, *Nat. Commun.* **2021**, *12*, 7311.

[48] Y. Gao, J. Shi, D. Yuan, B. Xu, *Nat. Commun.* **2012**, *3*, 1033.

[49] M. T. Jeena, L. Palanikumar, E. M. Go, I. Kim, M. G. Kang, S. Lee, S. Park, H. Choi, C. Kim, S. M. Jin, S. C. Bae, H. W. Rhee, E. Lee, S. K. Kwak, J. H. Ryu, *Nat. Commun.* **2017**, *8*, 26.

[50] S. Blockhuys, P. Wittung-Stafshede, *Int. J. Mol. Sci.* **2017**, *18*, 871.

[51] Y. Liu, J. Wang, M. Jiang, *Front. Immunol.* **2023**, *14*, 1145080.

[52] B. Chen, W. Le, Y. Wang, Z. Li, D. Wang, L. Ren, L. Lin, S. Cui, J. J. Hu, Y. Hu, P. Yang, R. C. Ewing, D. Shi, Z. Cui, *Theranostics* **2016**, *6*, 1887–1898.

[53] E. C. A. Eleutherio, R. S. S. Magalhães, A. A. Brasil, J. R. M. Neto, L. H. Paranhos, *Arch. Biochem. Biophys.* **2021**, *697*, 108701.

[54] P. C. Wong, D. Waggoner, J. R. Subramaniam, L. Tessarollo, T. B. Bartnikas, V. C. Culotta, D. L. Price, J. Rothstein, J. D. Gitlin, *PNAS* **2000**, *97*, 2886–2891.

[55] J. A. Tainer, E. D. Getzoff, J. S. Richardson, D. C. Richardson, *Nature* **1983**, *306*, 284–287.

[56] S. Stoll, A. Schweiger, *J. Magn. Reson.* **2006**, *178*, 42–55.

[57] S. Berg, D. Kutra, T. Kroeger, C. N. Straehle, B. X. Kausler, C. Haubold, M. Schiegg, J. Ales, T. Beier, M. Rudy, K. Eren, J. I. Cervantes, B. Xu, F. Beuttenmueller, A. Wolny, C. Zhang, U. Koethe, F. A. Hamprecht, A. Kreshuk, *Nat. Methods* **2019**, *16*, 1226–1232.

[58] C. A. Schneider, W. S. Rasband, K. W. Eliceiri, *Nat. Methods* **2012**, *9*, 671–675.

[59] Y. Cotte, F. Toy, P. Jourdain, N. Pavillon, D. Boss, P. Magistretti, P. Marquet, C. Depeursinge, *Nat. Photonics* **2013**, *7*, 113–117.

[60] J. L. Markley, A. Bax, Y. Arata, C. W. Hilbers, R. Kaptein, B. D. Sykes, P. E. Wright, K. Wüthrich, *J. Biomol. NMR* **1998**, *12*, 1–23.

[61] F. Crameri, G. E. Shephard, P. J. Heron, *Nat. Commun.* **2020**, *11*, 5444.